Physics-based model reconciles caldera collapse induced static and dynamic ground motion: application to Kīlauea 2018

Taiyi Wang[1], Katherine Coppess[1], Paul Segall[1], Eric M Dunham[1], and William L. Ellsworth[1]

[1]Stanford University

November 22, 2022

Abstract

Inflationary deformation and very long period (VLP) earthquakes frequently accompany basaltic caldera collapses, yet current interpretations do not reflect physically consistent mechanisms. We present a lumped parameter model accounting for caldera block/magma momentum change, magma chamber pressurization, and ring fault shear stress drop. The effect of pressurizing a spheroidal chamber is represented as a tri-axial expansion source, and the combined caldera block/magma momentum change as a vertical single force. The model is applied to Kīlauea 2018 caldera collapse events, accurately predicting near field static/dynamic ground motions. In addition to the tri-axial expansion source, the single force contributes significantly to the VLP waveforms. For an average collapse event with fully developed ring fault, Bayesian inversion constrains ring fault stress drop to ~0.4 MPa and the pressure increase to ~1.7 MPa. That the predictions fit both geodetic and seismic observations confirms that the model captures the dominant caldera collapse mechanisms.

Physics-based model reconciles caldera collapse induced static and dynamic ground motion: application to Kīlauea 2018

Taiyi Wang[1], Katherine Coppess[2], Paul Segall[1], Eric M. Dunham[1,3], William Ellsworth[1]

[1]Department of Geophysics, Stanford University
[2]Department of Physics, Stanford University
[3]Institute of Computational and Mathematical Engineering, Stanford University

Key Points:

- Caldera block/magma momentum change and chamber pressurization parsimoniously explain co-collapse inflation and very long period events
- Coupled tri-axial expansion source and vertical single force arise in the point source limit, contributing to very long period waveforms
- Inversion constrains co-collapse shear strength drop, pressurization, and mass of caldera block/magma during Kīlauea's 2018 events

Abstract

Inflationary deformation and very long period (VLP) earthquakes frequently accompany basaltic caldera collapses, yet current interpretations do not reflect physically consistent mechanisms. We present a lumped parameter model accounting for caldera block/magma momentum change, magma chamber pressurization, and ring fault shear stress drop. The effect of pressurizing a spheroidal chamber is represented as a tri-axial expansion source, and the combined caldera block/magma momentum change as a vertical single force. The model is applied to Kīlauea 2018 caldera collapse events, accurately predicting near field static/dynamic ground motions. In addition to the tri-axial expansion source, the single force contributes significantly to the VLP waveforms. For an average collapse event with fully developed ring fault, Bayesian inversion constrains ring fault stress drop to ~ 0.4 MPa and the pressure increase to ~ 1.7 MPa. That the predictions fit both geodetic and seismic observations confirms that the model captures the dominant caldera collapse mechanisms.

Plain Language Summary

Episodic caldera collapses at basaltic volcanoes can be hazardous, and forecasting them requires correct interpretations of geophysical observations. We use a physics-based approach to explain caldera collapse induced ground motions, such as during the 2018 collapse of Kīlauea. We show that, the most fundamental physical mechanisms of caldera collapse involve a pressure increase in the underlying magma chamber, due to rapid reduction of its volume, and a time-varying force, due to the acceleration of caldera block/magma. The physics-based model will allow more accurate interpretations of seismic data collected from less well monitored caldera collapses.

Corresponding author: Taiyi Wang, `taiyi@stanford.edu`

1 Introduction

A major challenge in understanding episodic caldera collapse at basaltic shield volcanoes is relating geophysical observations to the collapse dynamics. Inflationary co-collapse deformation outside of collapsing calderas (e.g., Michon et al., 2009; Segall et al., 2020), recorded by Global Navigation Satellite Systems (GNSS) or tiltmeters, and very long period (VLP) events (e.g., Kumagai et al., 2001; Fontaine et al., 2019), captured by seismometers, are reported at nearly all basaltic caldera collapses. Separate analyses of co-collapse deformation and VLP events have led to significant insight into caldera collapse dynamics (Kumagai et al., 2001; Gudmundsson et al., 2016; Duputel & Rivera, 2019; Roman & Lundgren, 2021; Segall & Anderson, 2021). However, geodetic data often do not have the temporal resolution to capture transient dynamics of caldera collapse, and their interpretations have been limited to kinematic magma chamber-ring fault interactions. In contrast, VLP waveforms are typically analyzed with moment tensor inversions, which do not lead to unique physical interpretations, absent constraints from near-field geodetic observations. Because of these limitations, current interpretations of co-collapse static and dynamic ground motions do not reflect mutually-consistent caldera collapse dynamics. Understanding the underlying dynamics would aid in interpreting cases where only seismic data are available, and aid in forecasting future collapse behavior.

Simultaneous analyses of GNSS/tilt and VLP data can shed light on caldera collapse dynamics by including observations over a wide range of time (seconds to minutes) and spatial (near-field to regional) scales. A predictive model capable of simulating both static and dynamic ground motions is required for such analyses. Kumagai et al. (2001) first introduced a quantitative model to explain the inflationary deformation associated with caldera collapses at Miyakejima. More recent models build on Kumagai et al. (2001)'s effort to include rate-and-state friction on the ring fault (Segall & Anderson, 2021) and to describe the dynamics of collapse sequences (Roman & Lundgren, 2021). We aim to add additional physics to the dynamic model and provide a parsimonious explanation of co-collapse static/dynamic ground motion.

Here we extend the Kumagai et al. (2001) model to account for the momentum change of magma, which is accelerated by the rapid downward movement of the collapsing caldera block. We present analytical solutions for caldera block displacement, chamber pressure, and ring fault shear stress as a function of time. We then formulate pressure and shear stress changes as a time-varying tri-axial expansion source and a single force. For the expansion source, we utilize a moment tensor form consistent with spheroidal cavities of any aspect ratio under uniform pressurization (Eshelby, 1957). Lastly, we apply the proposed model in a joint inversion of co-collapse GNSS displacement offsets and VLP velocity waveforms to gain insight into Kīlauea's 2018 caldera collapse events.

2 Theory

2.1 A model for caldera collapse dynamics

Consider a caldera block idealized as a cylindrical "piston" with radius R, height L, and bulk density ρ_p (Fig. 1 a). Prior to a collapse event, the piston is in static equilibrium, where the gravitational force, F_g, is balanced by magma chamber pressure force at the bottom of the piston, F_p, and the shear force on the ring fault, F_s. For basaltic shield volcanoes, flank eruptions reduce chamber pressure, thereby increasing shear stress on the ring fault leading to collapse. When shear stress on the ring fault exceeds the static strength, collapse initiates. The caldera block accelerates downwards, resulting in a force of equal magnitude to its momentum change, but of opposite direction (upward) on the crust. The collapsing caldera rapidly reduces the chamber volume, pressurizing the underlying magma chamber. The pressure force on the caldera block then increases, which decelerates the caldera block. A deceleration is equivalent to an upward acceleration of the caldera block. Therefore, past the peak downward velocity, the net force on the crust points downwards. Eventually, when the caldera block arrests, static equilibrium is restored.

Assuming rigid body motion of the piston, and a surrounding stationary, rigid crust, the momentum balance for the piston is:

$$\begin{aligned} m\ddot{u} &= F_g + F_s + F_p \\ &= mg - (2\pi RL)\tau(t) - (\pi R^2)p(t) \end{aligned} \tag{1}$$

where the left hand side is piston momentum change, u is the time dependent displacement and over-dot indicating time derivatives. The mass of the piston is $m = \pi R^2 L\rho_p$. τ is the spatially averaged shear stress on the side of the piston and p is the chamber pressure at its bottom. Note that $p(t) = p_0 + \delta p(t)$, where p_0 is the background pressure (prior to collapse) and δp the perturbation due to collapse. Due to the short duration of collapse events, the change in magma mass during collapse is neglected. Also neglecting acoustic waves and tractions due to viscous flow, the co-collapse chamber pressure evolution including chamber storativity and magma momentum change is (Appendix A):

$$p = \frac{\pi R^2}{\beta V}u + \frac{\phi m_f}{\pi R^2}\frac{\partial^2 u}{\partial t^2} + p_0 \tag{2}$$

where β is total compressibility (chamber + magma), V chamber volume, ϕm_f the inertial mass of magma in the chamber. Eqn. 2 is based on an asymptotic expansion of the solution in powers of the small parameter $\omega H/c$, where ω is the angular frequency, H is the characteristic length scale of the chamber, and c the acoustic wave speed of the magma. The zeroth order effect is that of pressurization due to storage properties of the chamber. We also account for inertia of the magma, an effect that is second order in $\omega H/c$.

For a cylindrical chamber of the same radius as the piston, $\phi = 1/3$ (Eqn. A6). For spheroidal chambers, $\phi < 1/3$. Substituting Eqn. 2 into the momentum balance yields:

$$m'\ddot{u} + \frac{\pi^2 R^4}{\beta V}u = mg - (2\pi RL)\tau - (\pi R^2)p_0 \tag{3a}$$

$$m' = m + \phi m_f \tag{3b}$$

The inertia imparted by magma within the chamber acts as an extra mass added to the piston (Fig. 1 c). We employ simple static-dynamic friction:

$$\tau_{str} = f\sigma_n \tag{4a}$$

$$f = \begin{cases} f_s & \dot{u} = 0 \\ f_d & \dot{u} > 0 \end{cases} \tag{4b}$$

where σ_n is the spatially averaged effective normal stress on the ring fault. Once the piston starts moving at $t = 0$, the strength, τ_{str}, instantaneously drops from the static strength, $\tau^s_{str} = f_s\sigma_n$, to the dynamic strength, $\tau^d_{str} = f_d\sigma_n$. The co-collapse displacement $u(t)$ and perturbation pressure $\delta p(t)$ are found analytically, assuming $\tau = \tau^d_{str}$ for $0 < t < t_{max}$ (Eqn. B3b and Fig. 1 c). The shear stress change for $0 \le t \le t_{max}$, assuming zero acceleration at $t = 0, t_{max}$ is thus:

$$\delta\tau = (-\pi R^2\delta p - m'\ddot{u})/(2\pi RL). \tag{5}$$

2.2 Point source representation

We seek a point source representation of the caldera collapse dynamics, which enables forward predictions of associated ground motion. A point source representation is

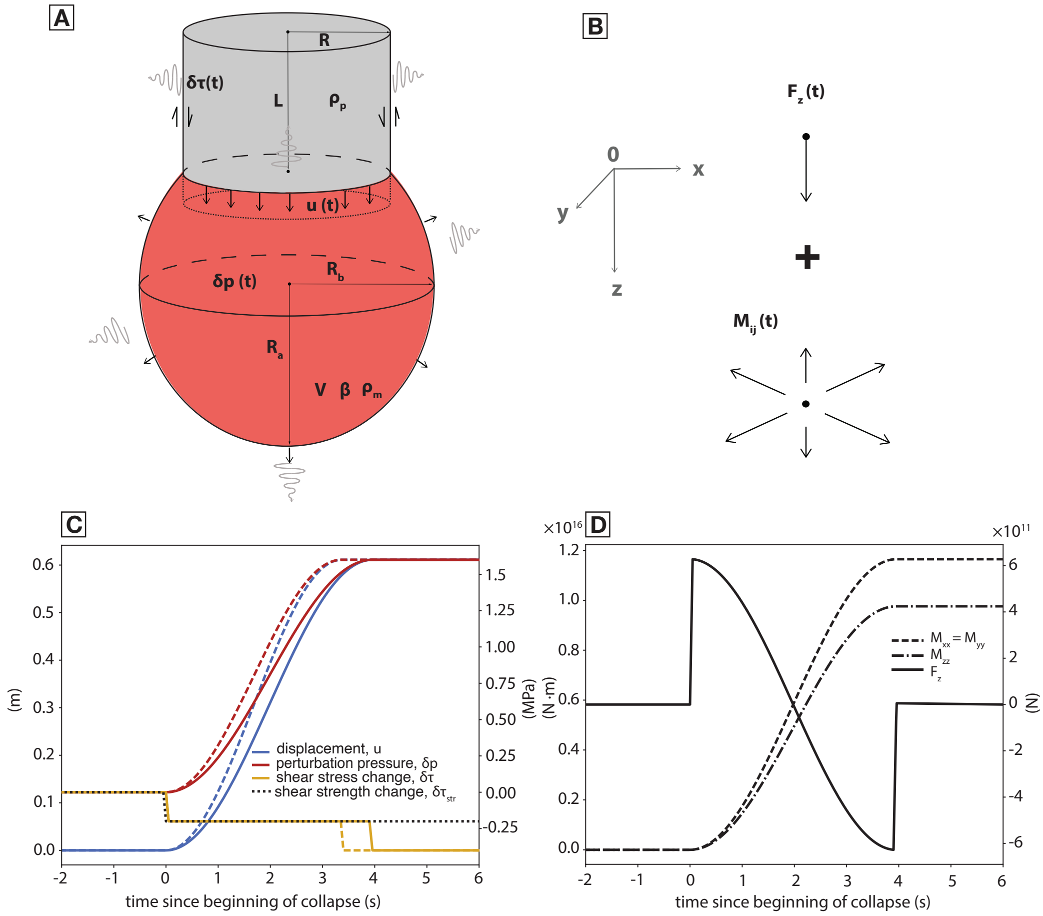

Figure 1: (a) Schematic of the caldera collapse model. Collapse block is idealized as an axially-symmetric piston bounded by a vertical ring fault. A vertically oriented, spheroidal chamber of aspect ratio α ($\alpha > 1$, prolate, $\alpha < 1$, oblate) is comprised of homogeneous, compressible magma bounded by elastic crust. (b) Coordinate system and the point source representation. Positive z axis points downward. $z = 0$ marks the piston bottom prior to collapse. Piston/magma momentum change and chamber pressurization are represented as a vertical single force and a point tri-axial pressure source, respectively. (c) Example solution to the momentum and mass balance equations. Solid lines show displacement, perturbation pressure, and shear stress, accounting for magma momentum change, which lengthens the collapse duration. Dashed lines show solutions without accounting for magma momentum change. Total shear stress drop is twice that of shear strength drop. (d) Corresponding time-dependent moment tensor components and vertical single force, for a chamber aspect ratio $\alpha > 1$.

justified when the wavelengths considered are long compared to source dimensions. Assuming a s-wave velocity of 3 km/s, the wavelength of typical VLP events, which have duration of $\sim$ 5 seconds, is of order 5 s $\times$ 3 km/s = 15 km, whereas the effective dimension of the source (basaltic magma chamber and piston) is $\sim$ 2 km. We thus use a tri-axial expansion point source to represent the pressure perturbation exerted on the magma chamber wall, and a vertical single force to represent the reaction force on the crust.

Pressurization of a spheroidal magma chamber can be represented by a tri-axial expansion source with moment tensor components, M_{ij}, which are derived by solving a system of equations involving the chamber aspect ratio, α, volume, V, and the pressure change, δp, given shear modulus μ and Poisson's ratio ν (Eshelby, 1957; Davis, 1986). Unbalanced forces give rise to momentum change, which is represented as a single force in the point source limit. The single force on the crust is of equal magnitude and opposite direction to the single force on the combined piston and magma mass, $F_z = -m'\ddot{u}$.

The dynamic displacement field is then computed by convolving the moment tensor, M_{ij}, and the vector single force, F_i, with the elastodynamic Green's functions G_{ij}:

$$u_i(\boldsymbol{x}, t) = \int_0^t M_{jk}(\boldsymbol{x}_0, t_0) \frac{\partial G_{ij}(\boldsymbol{x}_0, \boldsymbol{x}, t - t_0)}{\partial(\boldsymbol{x}_0)_k} dt_0 + \int_0^t F_i(\boldsymbol{x}_0, t_0) G_{ij}(\boldsymbol{x}_0, \boldsymbol{x}, t - t_0) dt_0 \quad (6)$$

where $i = x, y$ or z. $\boldsymbol{x}_0$, t_0 denote the source location and time, whereas $\boldsymbol{x}$, t denote the receiver location and time. Here $F_i = [0, 0, F_z]$. The static limit of the dynamic displacements for various chamber aspect ratios is verified (Fig. S3) using the semi-analytical Yang-Cervelli model (Yang et al., 1988; Cervelli, 2013).

3 Application to the 2018 collapse of Kīlauea caldera

3.1 GNSS and seismic data

We analyze near-field, co-collapse displacement offsets and VLP waveforms associated with the last 32 (of 62 total) collapse events, which are broader in scale, and occurred along a relatively well developed ring fault system. We use the displacement offsets and uncertainties computed by Segall et al. (2020). Offsets are determined as the difference between GNSS averaged positions (5 s solutions, stacked over 32 events) before and after a collapse event. We used a selection of 3 accelerometers (HMLE, PAUD, and RSDD) maintained by the National Strong Motion Project and 3 broadband seismometers (MLOD, HLPD, and STCD) maintained by the Hawaii Volcano Observatory for VLP waveform analyses (Fig. 2 a). For the accelerometers, we stack the waveforms from each component for the last 32 events, deconvolve the instrument response, integrate to velocity, and low-pass filter at a period of 5 seconds. Broadband velocity waveforms were processed similarly without integration in time.

3.2 Velocity model

We adopt a homogeneous half-space model of Kīlauea, assuming a s-wave velocity of $c_s = 1$ km/s, a p-wave velocity of $c_p = 1.7$ km/s, and an extra-caldera crustal density of $\rho_c = 3000$ kg/m^3 (justification in Section S3). Green's functions are generated using the FK method (Zhu & Rivera, 2002). Co-collapse displacement offsets are obtained by taking the limit $t \to \infty$.

3.3 Bayesian inversion

We employ a Bayesian framework to estimate the posterior probability density function (PDF) of the model parameters $\Delta\tau_{str}$, V, β, ρ_p, $\phi\rho_f$, R, and α, while fixing the depth and centroid location of the underlying Halemaʻumaʻu chamber to the median estimate

Parameters	**Symbol**	**Unit**	**Bounds on the uniform portion of prior**	**MAP model**	**90% confidence interval**
In inversion					
shear strength drop	$\Delta\tau_{str}$	MPa	[0.1, 1.3]	0.19	[0.19, 0.21]
piston radius	R	km	[0.5, 1.3]	0.45	[0.38, 0.57]
chamber volume	V	km^3	[2.5, 7.2]	4.6	[3.4, 7.2]
total compressibility	β	Pa^{-1}	$[10^{-9.70}, 10^{-8.88}]$	$10^{-9.73}$	$[10^{-9.81}, 10^{-9.53}]$
piston density	ρ_p	$kg \cdot m^{-3}$	[2400, 2800]	2500	[2350, 2820]
effective magma density	$\phi\rho_f$	$kg \cdot m^{-3}$	[210, 870]	170	[30, 260]
chamber aspect ratio [1]	α	-	[1.0, 1.4]	0.88	[0.88, 0.89]
Fixed					
crustal shear modulus	μ	GPa	3		
Poisson's ratio	ν	-	0.25	-	-
crustal density outside of caldera	ρ_c	$kg \cdot m^{-3}$	3000	-	-

[1] $\alpha > 1$ and $\alpha < 1$ indicate prolate and oblate, respectively.

Table 1: Model parameters, bounds on the uniform portion of prior, MAP model, and 95% confidence interval. The chamber centroid is fixed at the following longitude, latitude, and depth from surface: 155.278 °W , 19.407 °N, 1.94 km. Piston height, L, is defined as the depth to chamber centroid, subtracting chamber semi-major axis length.

of Anderson et al. (2019) (Table 1, also discussion in Section S5):

$$P(\boldsymbol{m}|\boldsymbol{d}) \propto P(\boldsymbol{d}|\boldsymbol{m})P(\boldsymbol{m}) \tag{7}$$

where $\boldsymbol{m}$ denotes model parameters and $\boldsymbol{d}$ the data. This equation states that the probability of a model conditioned on data, $P(\boldsymbol{m}|\boldsymbol{d})$ (posterior), is proportional to the product of the likelihood, $P(\boldsymbol{d}|\boldsymbol{m})$, and the prior distribution of the model parameters, $P(\boldsymbol{m})$. We employ a Gaussian-tailed uniform prior distribution (Table 1), where the standard deviation of the tail is 1/10 the width of the uniform part of the distribution (Anderson & Poland, 2016). The posterior probability density function (PDF) is estimated by an affine-invariant ensemble sampler for Markov Chain Monte Carlo (MCMC) (Foreman-Mackey et al., 2013). A detailed discussion on choice of covariance matrices can be found in Section S7.

Models were restricted to those with a collapse duration of $2-8$ seconds, ring fault slip of $2-5$ meters, and pressure increase of $0.5-4$ MPa. A pressure increase of $1-3$ MPa was estimated by Segall et al. (2020). GNSS station CALS, located on the caldera block, indicates 2.4 ± 0.4 m of co-collapse slip during a $5-10$ s period (Segall & Anderson, 2021). In trial inversions, magma momentum change appears to be of minor importance compared to that of caldera block, so we only used caldera block momentum change in generating forward predictions of the single force induced ground motions.

3.4 Results

The maximum a-posteriori (MAP) model not only generates predictions consistent with the duration and magnitude of the collapse, but also explains 67% of the variance in the static displacements and 64% of the variance in the VLP velocity waveforms (Fig. 2 b, c). Over-prediction of vertical static displacement is consistent with an oblate chamber geometry (discussed in Section 4.3). The fit to waveform relative phase amplitude is rather good, with exceptions at station HLPD and MLOD, which may be due to unaccounted-

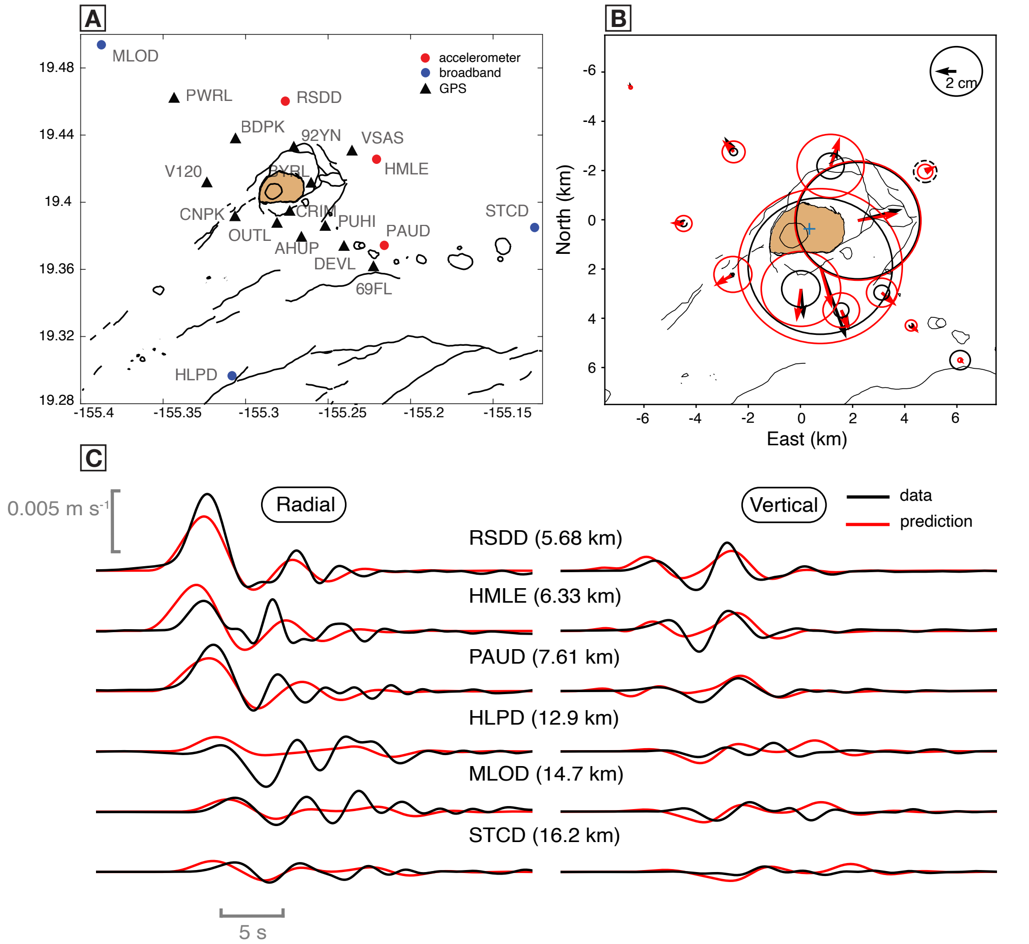

Figure 2: Comparison of observed and predicted static displacement and dynamic velocity waveform. (a) Map of accelerometers, broadband seismic stations, and permanent GNSS stations at Kīlauea summit, with pre-collapse caldera boundary. 2018 collapse structure is shaded. (b) fit to the GPS data with Maximum a-posterior (MAP) model, with radial component in arrows and vertical component in circles. Blue cross marks the location of Halemaʻumaʻu chamber centroid. (c) fit to the VLP velocity wave forms low pass-filtered at 5 s.

for elastic heterogeneities. The MAP model (Table 1) corresponds to a collapse duration of 7 s, a collapse magnitude of 2.3 m, and a pressure increase of 1.7 MPa.

4 Discussion

4.1 Caldera collapse dynamics and model assumptions

In the idealized model, collapse dynamics is fully described by the characteristic length, time, pressure, and a dimensionless stress drop parameter (Appendix B), the relationships of which are akin to those proposed by Kumagai et al. (2001): larger chamber volume, higher total compressibility (magma+chamber), or larger caldera block mass, extends the duration of caldera collapse with a square root dependence, and increases total slip on the ring fault linearly. One contribution of this study is to recognize that, downward displacement of the caldera block necessitates magma movement in the underlying chamber. The movement of magma imparts extra inertia to the caldera block (Eqn. 3 b), which slows its downward movement. Depending on the exact geometry of the magma chamber, the inertial effect may have varying degrees of importance. Future studies of caldera collapse should consider the inertial effects of magma movement on caldera collapse dynamics.

The model makes several assumptions regarding caldera collapse dynamics. Notably, instantaneous drop in shear strength on the ring fault and negligible radiated energy loss are assumed. The absence of pre-collapse acceleration of deformation suggests that the slip evolution distance, d_c, is less than 10 mm (Segall & Anderson, 2021). Compared with observed co-collapse slip of $\sim$ 2.5 m, such d_c is consistent with an almost instantaneous drop in fault strength, leading to negligible fracture energy.

We assess the contribution of radiated energy to caldera collapse dynamics by comparing the magnitude of the radiated energy, E_r (Eqn. 8), to the change in piston gravitational potential, the dominant term in the piston-chamber energy balance (Eqn. S4). Energy, being quadratic in far-field velocities, does not obey superposition of radiated energy from moment and force sources calculated separately. However, given that our goal is to obtain an order of magnitude estimate, we simply add the two energies (derivation in Appendix C):

$$\begin{aligned}E_r = &\frac{1}{60\pi\rho c_p^5}\int_0^\infty 3\ddot{M}_{xx}^2 + 3\ddot{M}_{yy}^2 + 3\ddot{M}_{zz}^2 + 2\ddot{M}_{xx}\ddot{M}_{yy} + 2\ddot{M}_{yy}\ddot{M}_{zz} + 2\ddot{M}_{xx}\ddot{M}_{zz}dt\\ &+ \frac{1}{30\pi\rho c_s^5}\int_0^\infty \ddot{M}_{xx}^2 + \ddot{M}_{yy}^2 + \ddot{M}_{zz}^2 - \ddot{M}_{xx}\ddot{M}_{yy} - \ddot{M}_{xx}\ddot{M}_{zz} - \ddot{M}_{yy}\ddot{M}_{zz}dt\\ &+ \frac{1}{12\pi\rho c_p^3}\int_0^\infty \dot{F_z}^2 dt\\ &+ \frac{1}{6\pi\rho c_s^3}\int_0^\infty \dot{F_z}^2 dt\end{aligned} \tag{8}$$

where c_p, c_s, ρ, are p-wave velocity, s-wave velocity, and crustal density. Here moment and force components are time dependent. Note that s-wave radiated energy for the moment tensor vanishes in the isotropic limit ($\ddot{M}_{xx} = \ddot{M}_{yy} = \ddot{M}_{zz}$), as expected. The change in gravitational potential is $E_g = mg\Delta u$. For the MAP model at Kīlauea, the radiated energy (2.2×10^{12} J) is $\sim$ 5% the change in gravitational potential (3.5×10^{13} J). This justifies neglecting the radiated energy in the momentum balance (Eqn. 3), and is expected to hold true for other caldera collapses. Neglecting fracture and radiated energy results in full dynamic overshoot. Thus, the quasi-dynamic shear stress decreases twice, at $t = 0$ and $t = t_{max}$ (Fig. 1 c), both of which are equal to the static-dynamic strength drop: $\Delta\tau_{str} = \tau_{str}^s - \tau_{str}^d = (f_s - f_d)\sigma_n$.

4.2 Coupled expansion source-single force and their contributions to observables

The tri-axial expansion source represents co-collapse pressurization of the chamber, contributing to both static and dynamic ground motions. Co-collapse inflation caused by chamber pressurization persists long after the end of each collapse event, because pressure reduction due to magma outflow occurs on a longer time scale than the collapse itself. Therefore, in the point source representation, the moment tensor components of the expansion source have ramp-like time dependence (Fig. 1 d). Although the moment history represents a monotonic increase in chamber pressure, convolution with elastodynamic Green's functions produces dynamic ground motions (Fig. 3 b).

The vertical single force represents momentum change of the caldera block/mobilized magma. It contributes to the dynamic ground motions, but not the static, extra-caldera inflationary deformation, in the limit of constant chamber mass during collapse. The sin-

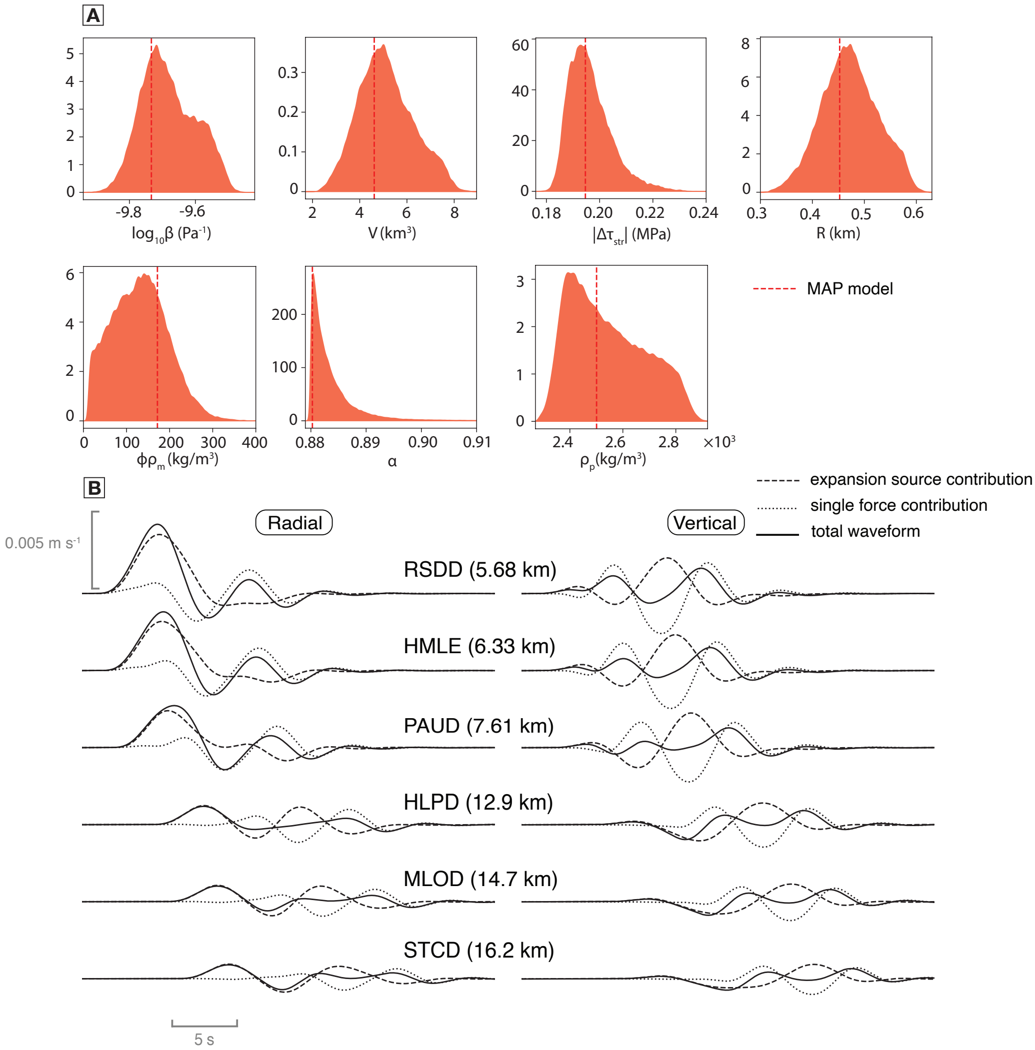

Figure 3: (a) Posterior probability density functions (PDFs) of the Bayesian Markov Chain Monte Carlo (MCMC) inversion after 1×10^6 iterations. MAP model denoted with vertical dashed line. (b) Moment tensor and vertical single force contributions to the synthetic velocity waveforms. Moment and single force contributions are comparable in magnitude. Individual components and total waveforms are low-pass filtered at 5 s.

gle force has significant contributions to the VLP waveforms. As shown in Fig. 3 b, for Kīlauea's 2018 events and likely for caldera collapse in general, the magnitude of the single force contribution to the VLP waveform is comparable to the moment contribution. This demonstrates that, at least in the near field, kinematic moment tensor inversions not accounting for the single force could lead to biased results and interpretations. Furthermore, the single force and the expansion source are coupled through the pressure exerted at the bottom of the caldera block (Eqn. 3). Therefore, kinematic inversions that independently constrain moment tensors and single forces are inadequate in capturing the full caldera collapse dynamics.

Inversions accounting for both the expansion source and single force better constrain parameter space, as demonstrated in the scaling of maximum pressure change δp_{max}, and maximum vertical force $F_{z,max}$:

$$\delta p_{max} = -\frac{4L}{R}\Delta\tau_{str} \tag{9a}$$

$$F_{z,max} = \frac{2\pi RL}{\gamma}\Delta\tau_{str} \tag{9b}$$

where $\gamma = m'/m$. Therefore, a model that explains static displacement (only sensitive to δp_{max}) alone has complete trade off between L/R and $\Delta\tau_{str}$. A model that explains static/dynamic ground motions simultaneously is much better constrained. For instance, increasing $\Delta\tau_{str}$ from its optimum value would require a decrease in both RL/γ and L/R, which can only be achieved by decrease L. Therefore, in practice, prior constraints on L would greatly enhance constraints on all parameters.

4.3 Analyses of Kīlauea's 2018 caldera collapse

The near-field VLP waveforms at Kīlauea are highly sensitive to caldera-collapse dynamics (sensitivity analysis in Section S2). Among parameters that influence caldera collapse dynamics, co-collapse pressure increase and shear stress drop are of particular interest to hazard forecasting. The magnitude of co-collapse pressure increase influences the intensity of flank eruptions downstream of the reservoir (Patrick et al., 2019), whereas the magnitude of the shear stress drop is proportional to inter-collapse periods. At a 90% confidence interval, we estimate the co-collapse shear stress decrease by 0.37−0.42 MPa, with a corresponding pressure increase of 1.6−1.9 MPa, assuming MAP parameter value for R, V, and α (Table 1). Our inferred stress drop is higher than the 0.30–0.32 MPa reported by Roman and Lundgren (2021), although the pressure increase estimate is lower than the 3.3 MPa reported by Segall et al. (2019) for a vertical ring fault. The difference between our estimated co-collapse pressure increase and that of Segall et al. (2019) can be reconciled when considering that the larger chamber volume and more oblate chamber geometry inferred here trade off with a smaller pressure increase. An oblate chamber geometry allows a smaller pressure increase to produce comparable vertical displacement at the surface, provided that misfit in radial displacement is not significantly impacted. However, the oblate chamber geometry is inconsistent with those inferred from pre- and post-collapse (Anderson et al., 2019; Wang et al., 2021) geodetic inversions, which indicate prolate chamber geometry. This discrepancy is not yet fully understood. The inferred piston radius, R, is in the range of $0.38-0.57$ km, smaller than the $0.8-1.3$ km radii of the ring fault surface trace. This apparent discrepancy can be at least partially explained by the positive correlation between R and chamber volume, V, evident in both characteristic scales (Eqn. B1) and in correlation diagram (Fig. S7).

From the MAP model, we estimate that the mass of caldera block material involved in an average collapse is $\sim 1.6\times10^{12}$ kg. The inversion indicates that equivalent to $\sim 8\times10^{11}$ kg of magma inertial mass was transiently mobilized by the descending caldera block, which represents $\sim 7\%$ of the inferred total magma mass in the Halemaʻumaʻu reservoir, assuming the MAP chamber volume of 4.6 km^3 and bulk magma density of

$2500\ \mathrm{kg}\cdot\mathrm{m}^{-3}$. Small mass fraction of mobilized chamber magma potentially reflects the complex geometry of the reservoir.

The proposed model provides a parsimonious explanation for both co-collapse static inflation and the VLP ground motions. Other potential mechanisms, such as slip on a non-vertical ring fault, have been suggested by moment tensor inversions (Lai et al., 2021) and theoretically shown to be resolvable at teleseismic distances (Sandanbata et al., 2021). However, our model's accurate prediction of static displacement and VLP waveforms at Kīlauea suggest that, first order physics (caldera block/magma momentum change and chamber pressurization) likely dominates caldera collapse dynamics.

5 Conclusions

- A dynamic model based on first-order caldera collapse physics provides a parsimonious explanation for co-collapse static inflation and VLP ground motions
- Co-collapse static inflation reflects chamber pressurization (represented as tri-axial expansion source), whereas VLP waveforms reflect time dependent caldera block/magma momentum change (represented as vertical single force), in addition to chamber pressurization
- Kinematic moment tensor or moment tensor + single force inversion can be biased given the coupled nature of expansion source and single force, whereas modeling of static displacement neglects additional constraints on parameter space due to caldera block/magma momentum change
- For an average caldera collapse event at Kīlauea in 2018, inversion suggests ring fault strength decrease of 0.19 MPa, chamber pressure increase of 1.7 MPa, mobilized crustal mass of 1.6×10^{12} kg, and mobilized magmatic inertial mass of 8×10^{11} kg.

Acknowledgement

This project was supported by National Science Foundation (NSF) grant EAR-2040425 and EAR-1930979.

Data Availability Statement

GNSS data are available through UNAVCO archive (https://www.unavco.org/data/data.html). Accelerometer and broadband data are available through the Incorporated Research Institute for Seismology (IRIS) Data Management Center (http://ds.iris.edu/ds/nodes/dmc/data/types/waveform-data/).

Appendix A Effect of magma inertia on acoustic impedance

A 1D analysis for the effective impedance of the chamber generates insight of magma inertial effect on piston movement, neglecting fluid viscosity. We consider a vertically oriented, cylindrical chamber of length, H, and cross sectional area, $\mathcal{A}$. The chamber has rigid walls, and is filled with compressible magma. The base of the piston is at $z = 0$ (same coordinate system as in Fig. 1 b). Fluid particle motion is constrained to the z direction. The goal is to obtain a relationship between magma inertia, magma storativity, and chamber pressure.

In the frequency domain, the plane wave solution for pressure perturbation is:

$$\delta\hat{p}(z,\omega) = \hat{a}\cos\left(\frac{\omega z}{c}\right) + \hat{b}\sin\left(\frac{\omega z}{c}\right) \tag{A1}$$

where c is magma acoustic wave speed. $\hat{a}$ and $\hat{b}$ are unknown coefficients determined by boundary conditions. Substitute pressure perturbation into the Euler equation in the frequency domain, $\rho i\omega\hat{v} = \partial\hat{p}/\partial z$ (note the material derivative in the Euler equation is simplified to a time derivative due to the large magnitude of acceleration compared to spatial variations in particle velocity), we obtain particle velocity:

$$\hat{v}(z,\omega) = \frac{i\hat{a}}{\rho c}\sin(\frac{\omega z}{c}) - \frac{i\hat{b}}{\rho c}\cos(\frac{\omega z}{c}) \tag{A2}$$

Apply the zero velocity boundary condition at $z = H$ yields $\hat{b} = \hat{a}\tan(\omega H/c)$. Next compute the hydraulic impedance (ratio of perturbation pressure over volume flow rate), $\hat{Z}$, at $z = 0$. The sine terms vanish at $z = 0$, and the result depends on $\hat{b}/\hat{a}$:

$$\hat{Z}(0,\omega) = \frac{\delta\hat{p}(0,\omega)}{\hat{v}(0,\omega)\mathcal{A}} = \frac{\rho c}{-i\tan(\frac{\omega H}{c})\mathcal{A}} \tag{A3a}$$

$$\cot(\frac{\omega H}{c}) = \frac{c}{\omega H} + \frac{\omega H}{3c} - \frac{1}{45}(\frac{\omega H}{c})^3 \tag{A3b}$$

We expand the cotangent term in the impedance with regard to $\omega H/c$ using Taylor series and keep terms up to order two, justified in the low frequency limit. We then recognize the chamber storativity, $S = (\mathcal{A}H)/\rho c^2 = \beta_m V$, and fluid mass, $m_f = \rho H\mathcal{A}$, embedded in the impedance expression:

$$\hat{Z}(0,\omega) = \frac{i\rho c^2}{\mathcal{A}\omega H} - \frac{i\rho\omega H}{3\mathcal{A}} \tag{A4a}$$

$$= \frac{1}{-i\omega S} + \frac{-i\omega m_f}{3\mathcal{A}^2} \tag{A4b}$$

We can now invert the impedance to time domain:

$$\delta\hat{p} = (\frac{1}{-i\omega S} + \frac{-i\omega m_f}{3\mathcal{A}^2})\hat{v}\mathcal{A} \tag{A5a}$$

$$-i\omega\delta\hat{p}S = (1 + \frac{(-i\omega)^2 m_f S}{3\mathcal{A}^2})\hat{v}\mathcal{A} \tag{A5b}$$

$$S\frac{\partial\delta p}{\partial t} = v\mathcal{A} + \frac{m_f S}{3\mathcal{A}}\frac{\partial^2 v}{\partial t^2} \tag{A5c}$$

$$\frac{\partial\delta p}{\partial t} = \frac{v\mathcal{A}}{S} + \frac{m_f}{3\mathcal{A}}\frac{\partial^2 v}{\partial t^2} \tag{A5d}$$

The above equation indicates that, the downward displacement is impeded by not only the storativity of the chamber, but the inertia of the magma. Integrating both sides of Eqn. A5d in time, we obtain:

$$p = \frac{\pi R^2}{\beta_m V}u + \frac{m_f}{3\mathcal{A}}\frac{\partial^2 u}{\partial t^2} + p_0 \tag{A6}$$

where β_m is the compressibility of the magma. More generally, a linearization of the mass conservation equation for chambers of arbitrary geometry (e.g., Segall et al., 2001) leads to $\frac{\pi R^2}{\beta V}u$, where β is the total compressibility. The inertial correction in the above equation can be generalized to chambers of arbitrary geometry, provided that the factor of 1/3 be replaced by an appropriate one.

Appendix B non-dimensional solutions

To better understand the dynamics, we nondimensionalize Eqn. 3 using the following characteristic time, pressure, and length:

$$t^* = \sqrt{\frac{\beta V m'}{\pi^2 R^4}} \tag{B1a}$$

$$p^* = \frac{m'g}{\pi R^2} \tag{B1b}$$

$$l^* = \frac{\beta V m' g}{\pi^2 R^4} \tag{B1c}$$

The momentum balance equation then becomes:

$$\ddot{\hat{u}} + \hat{u} = \pi_0 \tag{B2a}$$

$$\pi_0 = \frac{1}{m'g}(mg - 2\pi RL\tau^d_{str} - \pi R^2 p_0) = -\frac{2\pi RL}{m'g}\Delta\tau_{str} \tag{B2b}$$

π_0 can be understood as the dimensionless magnitude of shear strength drop.

Setting initial displacement and velocity to zero, we solve the dimensionless momentum equation:

$$\hat{u} = \pi_0(1 - \cos\hat{t}) \tag{B3a}$$

$$\delta\hat{p} = \hat{u} \tag{B3b}$$

where we omit the spatially dependent inertial correction to the perturbation pressure due to the lumped parameter nature of the model. It follows that the duration and magnitude of collapses are:

$$\hat{t}_{max} = \pi \tag{B4a}$$

$$\hat{u}_{max} = 2\pi_0 \tag{B4b}$$

Appendix C Radiated energy from point source representation

We can compute the radiated energy from the point source representation, assuming homogeneous full space. The energy rate can be expressed as the integral of far field particle velocity with traction in the same direction over a sphere enclosing the source, following Aki and Richards (2002):

$$\dot{E}_{radiation} = \oiint v_i \sigma_{ij} n_j dS \tag{C1}$$

where $i, j = 1, 2, 3$, or equivalently, x, y, z. Note here the integration is over a sphere at radius r centered at the source ξ_i. n_j denotes the surface normal vector. Without loss of generality, let $\xi_i = [0, 0, 0]$ for convenience. Substitute traction $\sigma_{ij}n_j$ with the product of specific impedance and far field particle velocity yields:

$$\dot{E}_{radiation} = \oiint v_i \rho c v_i dS \tag{C2}$$

where c is either p-wave or s-wave velocity.

We then substitute in far-field p-wave and s-wave velocity induced by a point source moment tensor and a single force (Aki & Richards, 2002):

$$v_n^{m,p} = \frac{\gamma_n\gamma_p\gamma_q}{4\pi\rho c_p^3}\frac{1}{r}\ddot{M}_{pq}(t - \frac{r}{c_p}) \tag{C3a}$$

$$v_n^{m,s} = -(\frac{\gamma_n\gamma_p - \delta_{np}}{4\pi\rho c_s^3})\gamma_q\frac{1}{r}\ddot{M}_{pq}(t - \frac{r}{\beta}) \tag{C3b}$$

$$v_n^{f,p} = \frac{1}{4\pi\rho c_p^2}\gamma_n\gamma_p\frac{1}{r}\dot{F}_p(t - \frac{r}{c_p}) \tag{C3c}$$

$$v_n^{f,s} = -\frac{1}{4\pi\rho c_s^2}(\gamma_n\gamma_p - \delta_{np})\frac{1}{r}\dot{F}_p(t - \frac{r}{\beta}) \tag{C3d}$$

where the directional cosines are defined as $\gamma_i = (x_i - \xi_i)/|x_i - \xi_i|$. Superscripts m, f, p, s denote moment tensor source, single force source, p-wave, and s-wave, respectively. Source receiver distance is labeled as $r = |x_i - \xi_i|$. c_p and c_s are p-wave and s-wave velocities.

Given the assumption that spheroid chamber has its axes aligned with the axes of the coordinate system, the moment tensor is diagonalized. Also here only vertical single force is considered. These two assumptions greatly simplify the integration kernels for radiated energy rate:

$$
\begin{aligned}
v_i^{m,p} v_i^{m,p} &= \frac{1}{16\pi^2\rho^2 c_p^6 R^2}(\gamma_1^2 \ddot{M}_{11} + \gamma_2^2 \ddot{M}_{22} + \gamma_3^2 \ddot{M}_{33})^2 \\
v_i^{m,s} v_i^{m,s} &= \frac{1}{16\pi^2\rho^2 c_s^6 R^2}[\ddot{M}_{11}^2(-\gamma_1^4 + \gamma_1^2) + \ddot{M}_{22}^2(-\gamma_2^4 + \gamma_2^2) + \ddot{M}_{33}^2(-\gamma_3^4 + \gamma_3^2) \\
&\quad + \ddot{M}_{11}\ddot{M}_{22}(-2\gamma_1^2\gamma_2^2) + \ddot{M}_{11}\ddot{M}_{33}(-2\gamma_1^2\gamma_3^2) + \ddot{M}_{22}\ddot{M}_{33}(-2\gamma_2^2\gamma_3^2)] \\
v_i^{f,p} v_i^{f,p} &= \frac{1}{16\pi^2\rho^2 c_p^4 R^2}(\gamma_3 \dot{F}_3)^2 \\
v_i^{f,s} v_i^{f,s} &= \frac{1}{16\pi^2\rho^2 c_s^4 R^2}(-\gamma_3^2 + 1)\dot{F}_3^2
\end{aligned}
$$

The integration over the sphere benefits from the following Cartesian-spherical coordinate conversion: $\gamma_1 = \cos\theta\cos\phi$, $\gamma_2 = \cos\theta\sin\phi$, $\gamma_3 = \sin\theta$. Assuming a positive z axis in the vertical direction, θ is measured from negative z-axis to positive z-axis (0 to π) and ϕ counterclockwise from positive x-axis (0 to 2π). Lastly, integrate the radiation rate over time yields the total energy (Eqn. 8).

References

Aki, K., & Richards, P. G. (2002). Quantitative seismology. In (p. 76-77). Sausalito, California: University Science Books.

Anderson, K., Johanson, I., Patrick, M. R., Gu, M., Segall, P., Poland, M., … Miklius, A. (2019). Magma reservoir failure and the onset of caldera collapse at Kīlauea volcano in 2018. *Science*, *366*(6470).

Anderson, K., & Poland, M. (2016). Bayesian estimation of magma supply, storage, and eruption rates using a multiphysical volcano model: Kīlauea volcano, 2000–2012. *Earth and Planetary Science Letters*, *447*, 161–171.

Cervelli, P. (2013). Analytical expressions for deformation from an arbitrarily oriented spheroid in a half-space. *American Geophysical Union, Fall Meeting abstract, V44C-06*.

Davis, P. M. (1986). Surface deformation due to inflation of an arbitrarily oriented triaxial ellipsoidal cavity in an elastic half-space, with reference to Kīlauea volcano, Hawaii. *Journal of Geophysical Research: Solid Earth*, *91*(B7), 7429–7438.

Duputel, Z., & Rivera, L. (2019). The 2007 caldera collapse of Piton de la Fournaise volcano: Source process from very-long-period seismic signals. *Earth and Planetary Science Letters*, *527*, 115786.

Eshelby, J. D. (1957). The determination of the elastic field of an ellipsoidal inclusion, and related problems. *Proceedings of the royal society of London. Series A. Mathematical and physical sciences*, *241*(1226), 376–396.

Fontaine, F. R., Roult, G., Hejrani, B., Michon, L., Ferrazzini, V., Barruol, G., … others (2019). Very-and ultra-long-period seismic signals prior to and during caldera formation on La Réunion island. *Scientific reports*, *9*(1), 1–15.

Foreman-Mackey, D., Hogg, D. W., Lang, D., & Goodman, J. (2013). emcee: The mcmc hammer. *Publications of the Astronomical Society of the Pacific*, *125*(925), 306.

Gudmundsson, M. T., Jónsdóttir, K., Hooper, A., Holohan, E. P., Halldórsson, S. A., Ófeigsson, B. G., … others (2016). Gradual caldera collapse at Bárdarbunga volcano, Iceland, regulated by lateral magma outflow. *Science*, *353*(6296).

Kumagai, H., Ohminato, T., Nakano, M., Ooi, M., Kubo, A., Inoue, H., & Oikawa, J. (2001). Very-long-period seismic signals and caldera formation at Miyake Island, Japan. *Science*, *293*(5530), 687–690.

Lai, V. H., Zhan, Z., Sandanbata, O., Brissaud, Q., & Miller, M. S. (2021). Inflation and asymmetric collapse at Kīlauea summit during the 2018 eruption from seismic and infrasound analyses.

Michon, L., Villeneuve, N., Catry, T., & Merle, O. (2009). How summit calderas collapse on basaltic volcanoes: new insights from the April 2007 caldera collapse of Piton de la Fournaise volcano. *Journal of Volcanology and Geothermal Research*, *184*(1-2), 138–151.

Patrick, M. R., Dietterich, H. R., Lyons, J. J., Diefenbach, A. K., Parcheta, C., Anderson, K., … Kauahikaua, J. P. (2019). Cyclic lava effusion during the 2018 eruption of Kīlauea volcano. *Science*, *366*(6470).

Roman, A., & Lundgren, P. (2021). Dynamics of large effusive eruptions driven by caldera collapse. *Nature*, *592*(7854), 392–396.

Sandanbata, O., Kanamori, H., Rivera, L., Zhan, Z., Watada, S., & Satake, K. (2021). Moment tensors of ring-faulting at active volcanoes: Insights into vertical-clvd earthquakes at the Sierra Negra caldera, Galápagos Islands. *Journal of Geophysical Research: Solid Earth*, e2021JB021693.

Segall, P., & Anderson, K. (2021). Repeating caldera collapse events constrain fault friction at the kilometer scale. *Proceedings of the National Academy of Sciences*, *118*(30).

Segall, P., Anderson, K., Johanson, I., & Miklius, A. (2019). Mechanics of inflationary deformation during caldera collapse: Evidence from the 2018 Kīlauea eruption. *Geophysical Research Letters*, *46*(21), 11782–11789.

Segall, P., Anderson, K., Pulvirenti, F., Wang, T., & Johanson, I. (2020). Caldera collapse geometry revealed by near-field GPS displacements at Kīlauea volcano in 2018. *Geophysical Research Letters*, *47*(15), e2020GL088867.

Segall, P., Cervelli, P., Owen, S., Lisowski, M., & Miklius, A. (2001). Constraints on dike propagation from continuous gps measurements. *Journal of Geophysical Research: Solid Earth*, *106*(B9), 19301–19317.

Wang, T., Zheng, Y., Pulvirenti, F., & Segall, P. (2021). Post-2018 caldera collapse re-inflation uniquely constrains Kīlauea's magmatic system. *Journal of Geophysical Research. Solid Earth*, *126*, e2021JB021803.

Yang, X.-M., Davis, P. M., & Dieterich, J. H. (1988). Deformation from inflation of a dipping finite prolate spheroid in an elastic half-space as a model for volcanic stressing. *Journal of Geophysical Research: Solid Earth*, *93*(B5), 4249–4257.

Zhu, L., & Rivera, L. A. (2002). A note on the dynamic and static displacements from a point source in multilayered media. *Geophysical Journal International*, *148*(3), 619–627.

Supplementary Information for:

Physics-based model reconciles caldera collapse induced static and dynamic ground motion: application to Kīlauea 2018

Taiyi Wang[1], Katherine Coppess[2], Paul Segall[1], Eric M. Dunham[1,3], William Ellsworth[1]

[1]Department of Geophysics, Stanford University
[2]Department of Physics, Stanford University
[3]Institute of Computational and Mathematical Engineering, Stanford University

1 Energy balance for the lumped parameter model

The mechanical energy balance can be derived directly from the momentum balance. First multiply both sides of the momentum balance with piston velocity, $\dot{u}$:

$$\dot{u}(m'\ddot{u} + \frac{\pi^2 R^4}{\beta V}u) = \dot{u}(mg - (2\pi RL)\tau - (\pi R^2)p_0) \tag{1}$$

which can be written as:

$$\frac{\partial}{\partial t}(\frac{1}{2}m'\dot{u}^2) = \frac{\partial}{\partial t}(mgu) - [\frac{\pi^2 R^4}{\beta V}\frac{\partial}{\partial t}(\frac{u^2}{2}) + \pi R^2 p_0 \frac{\partial u}{\partial t}] - (2\pi RL)\tau\frac{\partial u}{\partial t} \tag{2}$$

The above expression has dimensions of energy per unit time. The terms on the left hand side correspond to rate of change in piston kinetic energy. The terms on the right hand side correspond to rate of change in gravitational potential, rate of change in elastic strain energy of chamber + internal energy of magma, and work done against friction, respectively. Integrate both sides in time to get mechanical energy balance:

$$mg\Delta u - [\frac{1}{2}\Delta u^2 \frac{\pi^2 R^4}{\beta V} + (\pi R^2)p_0\Delta u] - (2\pi RL)\tau_d\Delta u = 0 \tag{3}$$

Note kinetic energy term vanishes because piston velocity is at equilibrium at the beginning and end of the integration. Radiated energy and fracture energy are not included in this analysis, as discussed in the main text.

2 Sensitivity of simulated waveforms to model parameters

The simulated waveforms are sensitive to variations in each inverted parameters (Fig. S1). Notably, within a physically plausible range of parameter values, the simulated waveforms are highly sensitive to shear strength drop, $\Delta\tau_{str}$, total compressibility, β, effective magma density, $\phi\rho_f$, and piston radius, R. The apparent lack of sensitivity to chamber volume, V, chamber aspect ratio, α, and piston density, ρ_p, is due to the relatively small variations in parameter values (within one order of magnitude), as expected in nature. Note the relative lack of sensitivity to chamber aspect ratio in the waveforms is partially compensated by the high sensitivity of near-field static displacement to aspect ratios.

The dependence of waveform characteristics on each parameter can also be deduced from scaling relationships (Eqn. 9a, 9b, B1a-c, B2b in main text). For example, the increase of waveform duration with β, $\phi\rho_f$ correspond to longer characteristic time, t^*. Increase $\Delta\tau_{str}$ increases $F_{z,max}$, resulting in larger peak amplitude of velocity waveforms.

Corresponding author: Taiyi Wang, taiyi@stanford.edu

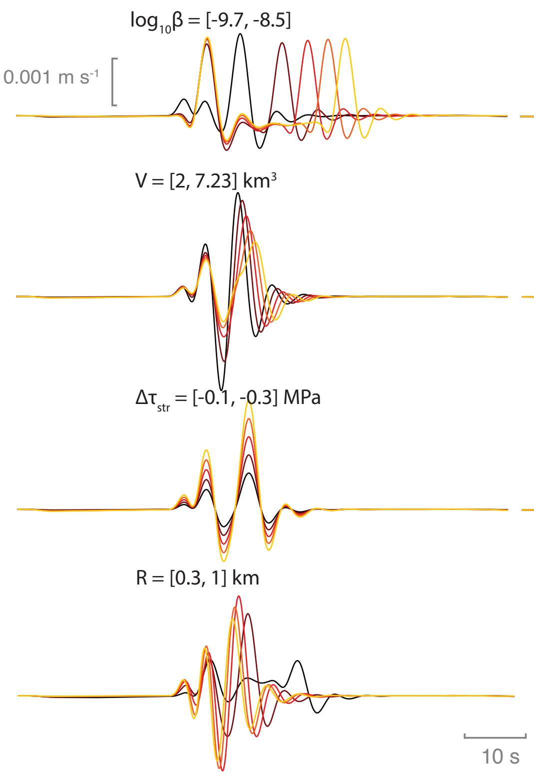

Figure S1: Sensitivity of simulated VLP waveforms to model parameters. Simulated vertical component velocity waveforms are shown with corresponding tested parameters. Values in brackets represent the lower and upper bounds of values tested. 5 evenly-spaced values are chosen within the bounds. Lighter color waveforms correspond to larger parameter values.

3 Velocity models of Kīlauea's summit

We opt to use a homogeneous half-space velocity model for computing synthetic seismograms. The reasoning is that common velocity models for Kīlauea's summit region (e. g. Lin et al., 2014) do not have fine enough resolution in the immediate proximity of the Halemaʻumaʻu magma chamber. Thus, seismic velocity models of Kīlauea tend to overestimate the crustal shear modulus due to spatial averaging of low-velocity zones near the chamber with high-velocity zones much farther away. In the absence of higher-resolution velocity model, we use a constant shear modulus of 3 GPa (Anderson et al., 2019), density of 3000 $\mathrm{kg \cdot m^{-3}}$, and a Poisson's ratio of 0.25 to compute for spatially uniform p and s wave velocities. At a period > 5 s, the VLP response is likely close to the quasi-static response of the earth, which justifies the low shear modulus used. Body wave scaling relationship indicates that increase μ decreases velocity waveform amplitude linearly, which biases estimated chamber pressure increase upwards. It is also shown that, although making the velocity below 3.5 km significantly faster (Fig. S2) elongates the simulated waveform in time (more pronounced in vertical component), the overall waveform shape does not change appreciably.

4 Validation of static limit deformation

The Eshelby solution for a moment tensor representing spheroidal cavities is derived in homogeneous full space (Eshelby, 1957). To ensure that the moment tensor is

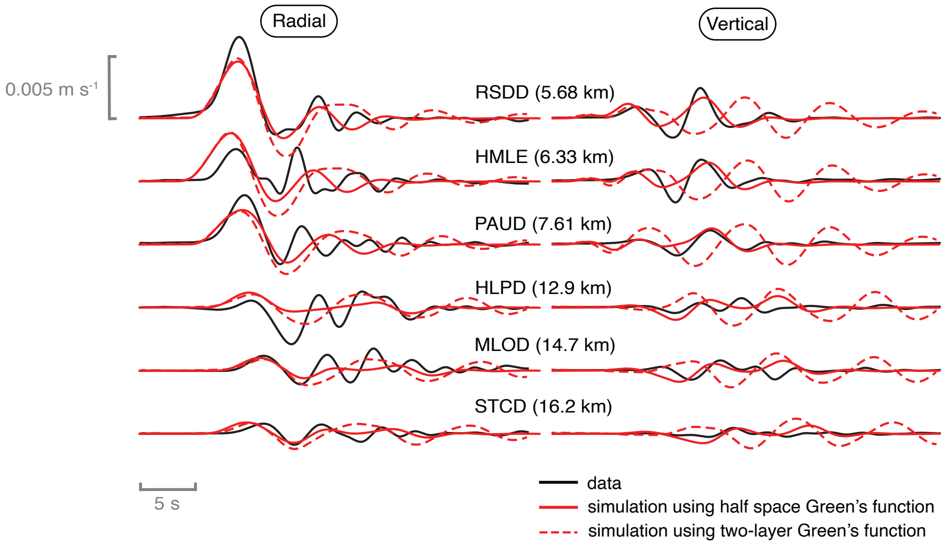

Figure S2: Comparing simulated waveforms with homogeneous half space model ($c_p = 1.73$ km/s and $c_s = 1$ km/s) and two layer model ($c_p = 1.73$ km/s and $c_s = 1$ km/s down to 3.5 km, below which $c_p = 5.5$ km/s and $c_s = 3.1$ km/s). At the stations' distances, adding a high velocity layer below 3.5 km elongates the simulated waveform in time.

adequate for centroid depths consistent with typical basaltic chambers, we compare the static deformation predicted using elasto-dynamic Green's functions with those predicted by the semi-analytical Yang-Cervelli model (Fig. S3). The results demonstrate that, for a large range of chamber aspect ratios, $0.2 - 1.4$, the Eshelby solution is adequate at a chamber centroid depth < 2.5 km.

5 Prior constraints

The characteristics of the simulated waveforms are dictated by both source dynamics and Green's functions, the latter of which are fixed to the assumed homogeneous velocity model. The dynamics of collapse is fully described by the dimensionless number π_0, and characteristic scales t^*, p^*, l^*. The simulated ground motions are also predicated on the crustal shear modulus μ, the Poisson's ratio, ν, and the chamber aspect ratio, α. A careful examination on the inter-dependence of the aforementioned parameters indicate that inverting the following parameters minimizes redundancy: $\Delta\tau_{str}$, V, β, ρ_p, $\phi\rho_f$, R, and α. In particular, the piston length, L, is not independent of chamber volume, V, and the chamber centroid depth, Δz: $L = \Delta z - (\frac{3V}{4\pi}\alpha^2)^{1/3}$, due to the assumption that the caldera block is directly situated above the chamber.

The choice of bounds on the uniform portion of Gaussian prior distributions is informed by previous studies. Surface expressions of the ring fault delineate a caldera block diameter varying between ~ 1.6 and 2.7 km. To account for uncertainties in subsurface ring fault geometry, we allow a prior range on ring fault radius, R, to vary between 0.5 and 1.3 km. The bulk density of typical basaltic rock in Hawaii averages at 2550 $\mathrm{kg \cdot m^{-3}}$ (Moore, 2001), so we consider $\rho_p = 2400 - 2800$ $\mathrm{kg \cdot m^{-3}}$. The ratio $\phi = 1/3$ is the upper bound on the percentage of magma in the chamber contributing to the total inertia of the system. Assuming that typical basaltic magma density is ~ 2600 $\mathrm{kg \cdot m^{-3}}$ and $\phi = 1/12 - 1/3$, we use an effective density of magma, $\phi\rho_f = 210 - 870$ $\mathrm{kg \cdot m^{-3}}$.

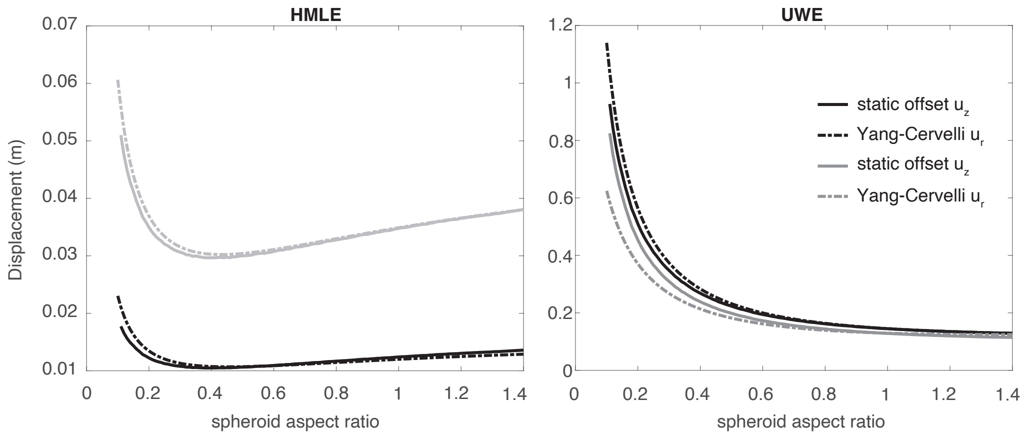

Figure S3: Simulated static surface displacements at various aspect ratios. left: (a) vertical and radial displacements at HMLE. (b) vertical and radial displacement at UWE. Vertical displacement in black; radial displacement in gray. Static limit of dynamic displacement in solid lines and Yang-Cervelli displacement in dashed lines. The results are computed with a pressure increase of 6.92 MPa, a chamber depth of 2.18 km, a chamber volume of 4 km^3, a crustal shear modulus of 3 GPa, and a Poisson's ratio of 0.25.

For the chamber volume, a 68% confidence interval, $V = 2.5 - 7.2$ km^3, estimated by Anderson et al. (2019), is used. We use a total reservoir compressibility of $\beta = 10^{-9.70} - 10^{-8.88}$ Pa^{-1}, where the upper bound is the upper 68% bound estimated by Anderson et al. (2019). Based on previous geodetic studies of the Halemaʻumaʻu reservoir, the chamber is expected to be a near spherical body, with an aspect ratio of $\alpha = 1 - 1.4$.

Total shear strength drop can be estimated from the pressure increase in the chamber after each collapse:

$$|\Delta\tau_{str}| = \frac{1}{2}\frac{\pi R^2 \Delta p}{2\pi RL} = \frac{R\Delta p}{4L} \tag{4}$$

where the shear strength drop is half of the total drop in stress, in the full dynamic overshoot limit. Co-collapse pressure increase, Δp, has been estimated to be 1−3 MPa (Segall et al., 2019). For a piston radius, $R = 500 - 1300$ m, and $L = 750 - 1200$ m, the shear strength drop needed to return the piston to static equilibrium is $0.1 - 1.3$ MPa.

6 Data covariance matrices

We assume that the data errors are normally distributed such that the likelihood function is:

$$P(\boldsymbol{d}|\boldsymbol{m}) = \prod_{i=GNSS,VLP} (2\pi)^{-N_i/2} det(\boldsymbol{C_i})^{-1/2} \times exp[-\frac{1}{2}(\boldsymbol{d_i} - \boldsymbol{G}(\boldsymbol{m}))^T \boldsymbol{C_i}^{-1}(\boldsymbol{d_i} - \boldsymbol{G}(\boldsymbol{m}))] \tag{5}$$

where the likelihood of both GNSS displacement offsets and VLP velocity waveforms are accounted for in the inversion. Here, N is the number of data points in each data set, $\boldsymbol{C}$ is the data covariance matrix, and $\boldsymbol{G}$ is the forward model operator.

The covariance matrices for both data sets are assumed to be diagonal (uncorrelated noise). GNSS uncertainties are propagated through stacking time series and differencing positions (Segall et al., 2020). VLP waveform uncertainties are set to a magnitude ensuring that, the weighted sum of squared residuals, $(\boldsymbol{d_i} - \boldsymbol{G}(\boldsymbol{m}))^T \boldsymbol{C_i}^{-1}(\boldsymbol{d_i} - \boldsymbol{G}(\boldsymbol{m}))$, is of order $N - M$, given a sampling rate (the weighted sum of square residuals follow a χ^2 distribution with $N - M$ degree of freedom, where N is the number of data points and M is the number of estimated parameters). Such an approach ensures that the magnitude of data uncertainties are not significantly under- or over- estimated. To account for the large number of waveform data points versus GNSS static offset data points, a trial-and-error weight is applied to the likelihood for the static offsets.

7 Parameter correlations

By design, the inverted parameters are rather independent of each other, and thereby lack correlations (Fig. S4). There is a weak, positive correlation between chamber volume, V, and total compressibility, β, the reason of which may not be immediately clear, given the typical trade off between V and β in volumetric sources. However, such behavior is explained by noting the nonlinear dependence of the characteristic scales (Eqn. B1a - B1c) on V, given $m' = m + \phi\rho_f V$. The positive correlation between piston radius R, and β (or V) potentially explains the apparent small radii estimated from inversion.

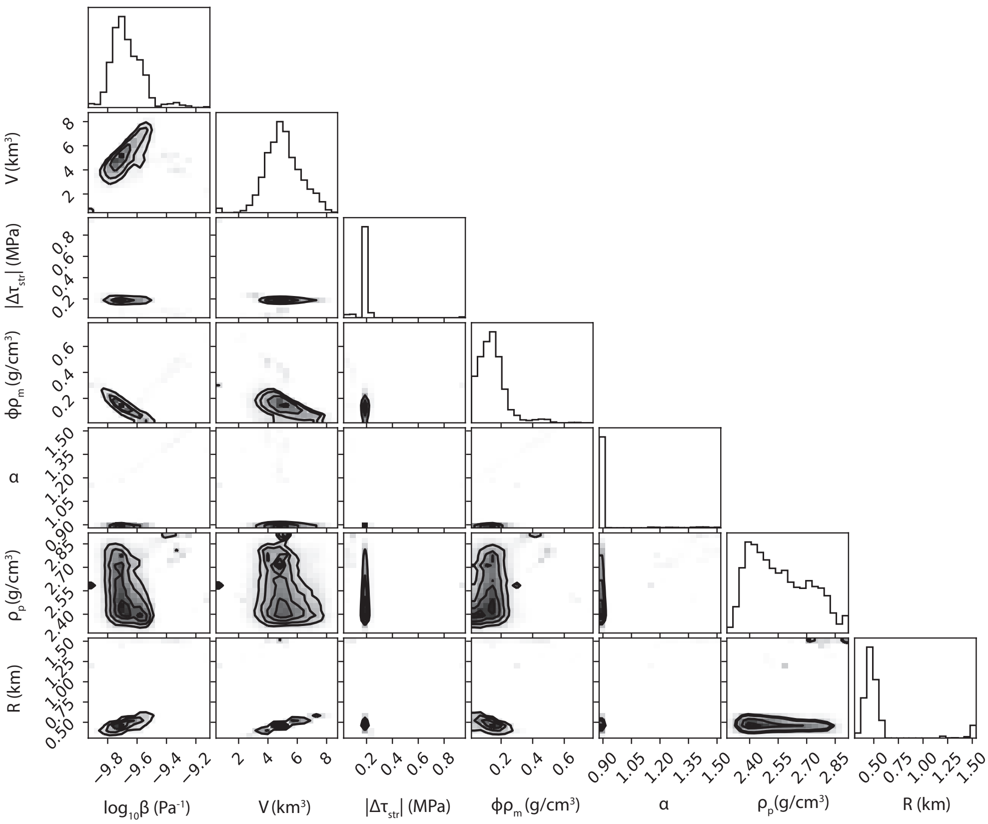

Figure S4: Correlation of inverted parameters. Parameters are mostly independent of each other, except chamber volume-compressibility and chamber volume-piston radius.

References

Anderson, K., Johanson, I., Patrick, M. R., Gu, M., Segall, P., Poland, M., ... Miklius, A. (2019). Magma reservoir failure and the onset of caldera collapse at Kīlauea volcano in 2018. *Science*, *366*(6470).

Eshelby, J. D. (1957). The determination of the elastic field of an ellipsoidal inclusion, and related problems. *Proceedings of the royal society of London. Series A. Mathematical and physical sciences*, *241*(1226), 376–396.

Lin, G., Shearer, P. M., Matoza, R. S., Okubo, P. G., & Amelung, F. (2014). Three-dimensional seismic velocity structure of Mauna Loa and Kīlauea volcanoes in Hawaii from local seismic tomography. *Journal of Geophysical Research: Solid Earth*, *119*(5), 4377–4392.

Moore, J. G. (2001). Density of basalt core from Hilo drill hole, Hawaii. *Journal of Volcanology and Geothermal Research*, *112*(1-4), 221–230.

Segall, P., Anderson, K., Johanson, I., & Miklius, A. (2019). Mechanics of inflationary deformation during caldera collapse: Evidence from the 2018 Kīlauea eruption. *Geophysical Research Letters*, *46*(21), 11782–11789.

Segall, P., Anderson, K., Pulvirenti, F., Wang, T., & Johanson, I. (2020). Caldera collapse geometry revealed by near-field GPS displacements at Kīlauea volcano in 2018. *Geophysical Research Letters*, *47*(15), e2020GL088867.